ISSN: 2993-8643

Research Article

Engineering: Open Access

Microstructural Study to Investigate Creep Properties of IMI685 Near Alpha Ti Alloy

Jayanthi A[1*], M. Anil Kumar[1] and B. Ravisankar[2]

[1]*Foundry and Forge Division, Hindustan Aeronautics Limited, Bangalore, Karnataka, India*

[2]*Department of Metallurgical and Materials Engineering, National Institute of Technology, Tiruchirappalli, Tamil Nadu, India*

[*]Corresponding Author
Jayanthi A, Development Department, Foundry and Forge Division, Hindustan Aeronautics Limited, Bengaluru -560017, Karnataka, India.

Submitted: 2026, Jul 17 **Accepted:** 2026, Aug 20; **Published:** 2026, Sep 01

Citation: Jayanthi, A., Anil Kumar, M, A., Ravisankar, B. (2026). Microstructural Study to Investigate Creep Properties of IMI685 Near Alpha TI Alloy. *Eng OA, 4*(9), 01-12.

Abstract

IMI 685 is a near alpha (α) titanium alloy used in compressor discs for aero engines due to its high creep resistance. This work mainly focuses on detailed microstructural study of a real forging of size ∅400 x 75mm height both in as forged and heat-treated condition. The forging was carried out in α + β(beta) region and β region. Creep properties at 520°C, stress of 300MPa for 100h duration were evaluated for both conditions and compared. The β forged forging showed higher creep resistance (0.06% plastic strain) than α + β forged forging (0.14% plastic strain) due to the difference in grain size and grain boundary thickness which is reflected in steady state creep rate also. The steady state creep rate was nearly 3 times higher in α + β forged compared to β forged suggesting forging at β region gives higher creep resistance.

Keywords: IMI 685, Creep Properties, Near Alpha Ti Alloy, Forging, Microstructural Studies

1. Introduction

Titanium alloys are used in gas turbine application due to its high strength to weight ratio, high mechanical properties, fatigue and creep properties. Major application of Ti alloys are in the area of fan blades, compressor discs, blades, etc.[1]. Titanium alloys are grouped into different categories depending on their crystal structure such as alpha(α) alloys containing hexagonal close packed (hcp) structure (e.g. Commercially pure Ti alloys with addition of oxygen, Ti-5Al-2.5Sn), beta(β) alloys contains body centered cubic (bcc) structure(e.g. Ti-13V-11Cr-3Al), near α alloys(e.g. IMI685, IMI 834, IMI 839), α + β alloys(e.g. Ti6Al-4V, Ti-6Al-6V-2Sn) and near β alloys(e.g. TIMETAL 10-2-3) containing a different proportion of hcp and bcc structure.

Ti-Al-Zr-Sn-Mo-Nb-Si Ti alloy system forms near α alloys. These alloys contain beta stabilizers (Mo, Si and Nb) less than 2 percent and Si up to 0.5 percent. These are used in high temperature applications up to 600°C due to the presence of silicides [2,3]. Near α alloys are used in compressor disc and blade applications in gas turbine engine for its excellent thermomechanical properties, creep resistance, high fatigue resistance, oxidation resistance and weldability [3]. Some of the near α alloys developed are IMI 679, IMI685, IMI834, IMI 829, Ti-811, Ti-1100, Ti-60, Ti-600, TA15[4].

IMI 685 alloy (Ti-6Al-5Zr-0.5Mo-0.25Si) is the first commercially used alloy in β solutionised condition in RB 21I, Rolls-Royce/ Turbomeca Adour, RB 199 and SNECMA M53 engines to obtain higher creep resistance [1,5]. The mechanical properties are affected by the morphology of α phase, grain size, α platelet thickness and distribution of phases in near α alloys which in turn are dependent on the prior thermomechanical working and heat treatment [5]. Creep resistance is higher in lamellar structure compared to equiaxed microstructure in α + β (beta) alloys due to the hcp crystal structure of the α phase and the addition of Si aids in segregating the dislocations which effectively prevents dislocation climb and improves the creep resistance and strength of this alloy [6].

Li et al., studied on the effect of initial non-uniform microstructure on the flow behavior and microstructure evolution of TA15 near α alloy. The work indicated that the lamellar alpha undergoes kinking and bending due to plastic buckling. Globularization of alpha during deformation is due to dynamic recrystallization and

bending of lamellar alpha [7]. The researchers also have studied on the hot deformation behavior of Ti-64 alloy with different starting microstructures and on the dependence of the flow softening mechanism on colony size, various initial microstructures, morphology of lamellar α, including initial lamellar α thickness and texture [8-12]. These works provide a detailed description for understanding the deformation behavior and microstructural features of Ti alloy and emphasis that all the above-mentioned factors are directly related to the mechanical properties of the Ti alloys.

Filip et al., studied the influence on the mechanical properties of the two phase Ti alloy with respect to microstructure and found that it is sensitive to the phases present, grain size and shape, distribution of phases and morphology [13]. Slow cooling from the β phase resulted in thick lamellar α while fast cooling resulted in martensitic microstructure and the width of α depends on the cooling rate as was observed by the Blenkinsop et al., (on 12mm thick forged billet) and Guo and Baker for IMI 685. Assadi et al., investigated the mechanism of creep behavior in near α Ti alloys in 387°C to 587°C and showed that two mechanisms are operating [14-16]. At low temperatures creep exhibits nearly athermal characteristics with very low apparent activation energy (~30 to 83kJ/mol). This corresponds to dynamic strain aging behavior and '*it is controlled by drag effect of solute atmospheres associated with moving dislocations*'[16]. At high temperatures creep is associated with microstructural changes such as '*stress-assisted precipitation occurring on dislocations during creep and it is proposed that the creep rate is limited by the rate at which the dislocations can break away from the precipitates*'[16].

Liu and Baker have studied on the hot deformation behavior of isothermal β forging of IMI 685 using ∅50mm x 50mm length in the temperature region of 1025°C to 1075°C and showed that dynamic recovery was predominant during forging. Guo and Baker used ∅50mm x 75mm length samples and studied on the grain growth and thermomechanical process at 970°C, 1000°C and 1050°C and found that above β transus temperature (BTT) the grain growth constant was three times higher than the grain growth constant in α + β temperature region [15,17]. Gopalakrishna et al., produced a process map for IMI685 in the temperature region of 775°C to 1025°C and indicated that superplastic forming was possible at lower temperature and lower strain rates [18].

Isothermal forging of compressor disc in LT26A (equivalent grade of IMI685) has been reported by Somani et al., in the α + β phase temperature range (similar configuration of forging presented in the paper) [19]. Upon comparison of mechanical properties with the similar IMI685 compressor disc whose manufacturing process was unknown have reported that there was no appreciable variation in room temperature and high temperature tensile values. However, the creep plastic strain was lower in LT26A compared to the other disc and attributed it to the heat treatment process and non-uniform grain size distribution (0.2 -1mm) over the cross section of the disc. Barbier et al., (sample size ∅240mm x 40mm thick – single stage upsetting) and Vassel et al., have carried out deformation at different temperature regions and concluded that room temperature mechanical properties were not affected by the forging temperature while the creep properties were affected significantly with respect to forging temperature and heat treatment temperature [20,21].

From the literature, it was found that studies have been carried out on sample level at different temperature region and one paper on large size compressor disc (where our organization was also part of development) using isothermal process in entirely α + β range [7-21]. However, an elaborate study on the effect of different forging temperature at different stages of forging on the component level has not been carried out. Hence, objective of this study is to understand the relationship between forging parameters and creep properties of IMI 685 compressor disc forging using non-isothermal forging route.

In this paper a detailed microstructural study has been carried out in the as forged condition and in the heat-treated condition on a compressor disc forging of size ∅400 mm x 75mm height using a different combination of α + β phase and β phase forging with three stages of forging. In addition, creep properties at 520°C at 300MPa for 100h have been evaluated. The forging sequence was finalized based on finite element analysis reported in our earlier publication [22]. The forging experiments were formulated based on the simulation studies and the quality requirement for the intended application. The present study aimed to establish the relationship between microstructure formed during forging and its effect on the creep properties so as to finalize the forging parameters to manufacture IMI685 large size forgings in non-isothermal forging.

2. Materials and Methods

IMI685 extruded material of ∅150 mm x 420 mm length was used for this study and its chemical composition (in wt.%) is 6.09Al-4.68Zr-0.57Mo-0.26Si-0.14O-0.04Fe-Ti. Figure 1 shows the forging process sequence. Forging temperatures for two trials are shown in Table 1. The billets were soaked for 2.5h to 3 h and dies were heated to 250°C and soaked for 5 to 6 h (soaking time selected based on the section thickness of the material) in an electrical resistance furnace. BTT for this alloy is 1020°C as provided by raw material manufacturer. Die material chosen was NCM (Nickel-Chrome-Molybdenum) die steel with hardness of 400 HB (Brinell hardness number). Upsetting operation was carried out using flat dies in the 30MN capacity hydraulic press. Mica sheets were used between the die and billet interface to reduce heat loss during upsetting operation. Based on the earlier forging simulation results, top and bottom surfaces were removed to avoid the dead zone [22]. Die forging using profile dies was carried out using a hammer capable of delivering 475 kJ per blow. Upsets were glass coated to improve lubrication and to avoid oxygen pickup before loading into the furnace. The forgings were cooled in the air after forging operation. Forged discs were pre-machined to satisfy the requirements of heat treatment (limiting section thickness for this material is 60mm[14]). The forgings were solutionised at 1050 °C for 1.5 h, quenched in oil followed by aging at 550°C for 24 h and cooled in air [23].

A 15mm thick slice of forging along grain flow direction (Figure 2a) has been cut using CNC wire cutting machine for microstructure mapping across the cross section of the forging. Seven places as shown in Figure 2b were chosen inside the sonic profile (Sonic profile is the intermediate machining profile used for checking the ultrasonic quality before the final component machining) from inner to outside of the forging for studying the variation of microstructure

Figure 1: Forging process sequence finalized using simulation studies. Upset 1 and 2 carried out in hydraulic press and die forging carried out in pneumatic hammer [22].

As the machined component will be realized using only the material available in sonic profile, microstructure study was restricted within the sonic profile. Microstructure samples were prepared as per ASTM E3, etched using Kroll's reagent as per ASTM E407 and analyzed using Leica Microscope up to 1000X magnification. The grains are approximately equiaxed and are coarser than ASTM grain size No.00. Hence, grain size was calculated by taking measurement of the length and breadth of individual grains covering a region of 10mm x 10mm cross section. The average diameter was arrived at based on the average length and breadth of the grains. SEM analysis for α morphology was carried out using Carl Zeiss make, EVO18 Research SEM.

Three samples for each experiment of specimen size of 15 mm square cross section x 100 mm length were extracted from the center of the disc as shown in Figure 2b through CNC wire cutting method for creep studies. Creep samples as per dimensions (∅6.18 mm) shown in Figure 3b were prepared using CNC machine and Figure 3a shows the machined creep sample. The equipment for creep testing, procedures for testing and data analysis were as per ASTM E139 standard. Constant load creep test was conducted in air at 520°C for 100 h and the plastic strain of E1 and E2 were studied and compared. The equipment used for creep testing was Microtest Creep testing machine as per the setup shown in Figure 3c. Three thermocouples at top, center and bottom of sample were positioned inside the heating zone of furnace along with extensometer. Two linear variable differential transducers (LVDTs) were attached to the extensometer for recording the change the length and average reading of both LVDTs was used for plotting the creep curve.

Experiment	Forging sequence	Forging Temperature
E1	Upset 1 Upset 2 Die forging	30°C below BTT 30°C below BTT 30°C below BTT
Upset 2	Upset 1 Upset 2 Die forging	30°C below BTT 30°C above BTT 30°C above BTT

Table 1: Forging Process Parameters

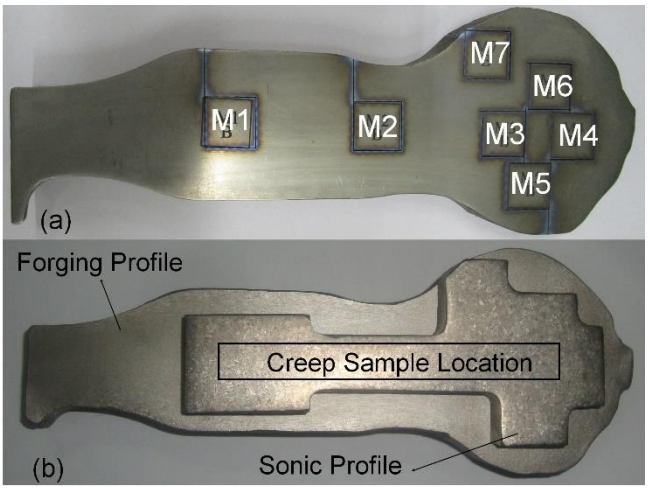

Figure 2:(a) Microstructure Sample Location (M1 to M7) Extracted from the 15mm Transverse Slice from the Forging and (b) Creep Sample Location Inside the Sonic Profile

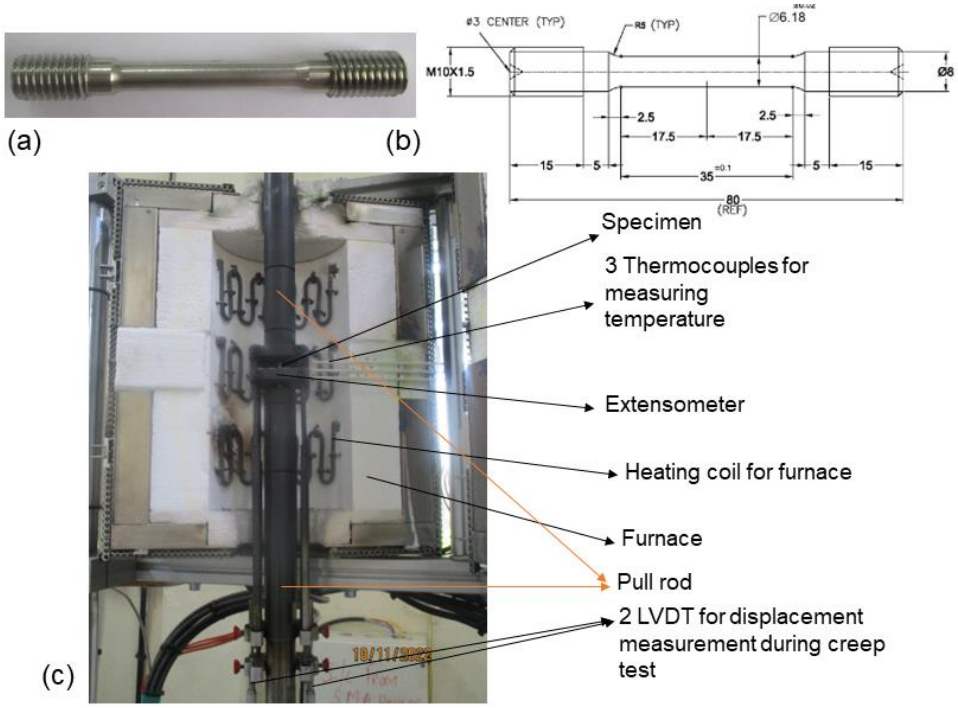

Figure 3: (a) Creep Sample with (b) Creep Sample Dimensions and (c) Creep Testing Arrangement

3. Results and Discussions

Element	Point 1 (wt%)	Point 2 (wt%)	Point 3 (wt%)	Point 4 (wt%)	Point 5 (wt%)	Point 6 (wt%)	Point 7 (wt%)
	Entire area	Area inside the α platelet			On grain boundary		
Ti	88.2	89.2	89.0	89.0	78.4	79.3	82.0
Al	5.5	6.2	6.1	6.2	2.9	4.3	3.0
Zr	5.2	4.3	4.5	4.4	9.5	6.5	8.3
Mo	0.7	0.1	0.1	0.1	8.8	9.6	6.6
Si	0.3	0.2	0.3	0.3	0.4	0.2	0.2

Table 2: EDAX Analysis Showing Chemical Composition at Different Locations

3.1. Raw Material Microstructure

Figure 4a shows the extruded raw material microstructure showing elongated lath primary β (width of 15 to 20 micron) with fine α at the interphase boundary. Figure 4b shows the SEM image with points for EDAX analysis. Figure 4c shows typical EDAX spectrum inside the α platelet and Figure 4d shows typical EDAX spectrum on the grain boundary. Table 2 shows the EDAX analysis of seven points covering the entire area, inside the grain and grain boundary. It was seen from the EDAX analysis, beta stabilizer especially Mo segregated along the grain boundary along with Zr during solidification, alpha stabilizer especially Al present inside the grain boundary and Si observed in both the areas.

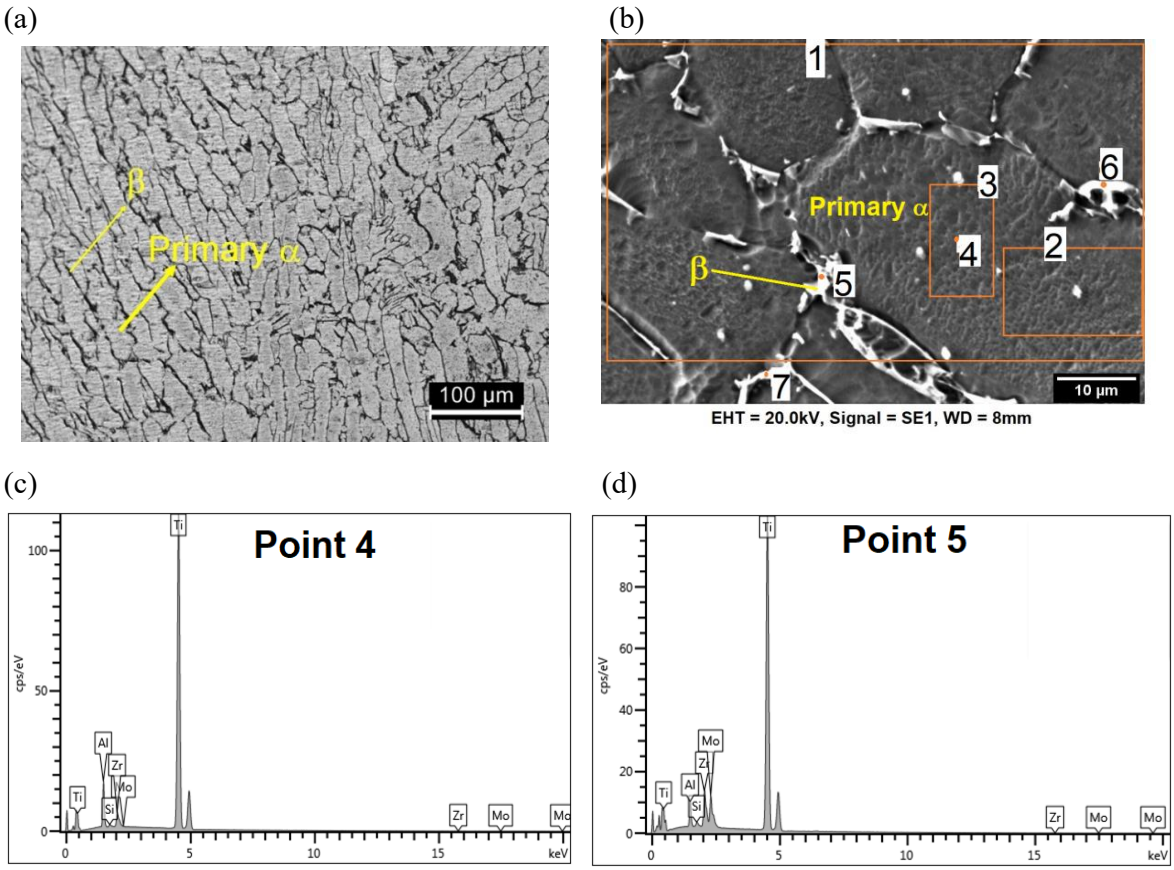

Figure 4: (a) Raw Material Microstructure Showing Elongated α Grain with β at the Grain Boundary, (b) SEM Image along with Locations for EDAX Analysis, (c) EDAX Spectrum within Elongated α Platelet Showing α Rich Elements and (d) EDAX Spectrum on the Grain Boundry Showing β Rich Elements

3.2. As Forged Microstructure

E1 condition shows elongated primary α deforming along the contour of the forging and smaller volume fraction of transformed α showing widmanstatten structure or aligned α platelets (Figure 5). Transformed α was seen near the grain boundaries due to the presence of β phase in the grain boundaries which act as nucleation sites for phase transformation. The similar microstructure was reported by Guo [15]. The kinking or bending of grains (Figure 5) and the flow of elongated α along the deformation were noticed in all the locations of the microstructure. The kinking of lamellar microstructure has been reported in literature for the transformation of Ti alloys below BTT hot working [24,25] due to the bending of lamellar α in the form of plastic buckling and not by a shear band or deformation band.

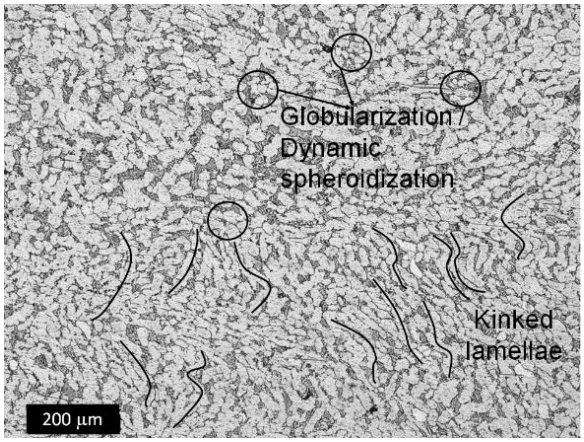

Figure 5: As Forged Microstructure of E1 Showing Kinking or Bending of α Laths (lines) and Globularization of α Laths (Circles)

In E2 condition, microstructure shows large equiaxed grains of transformed α formed on the prior β grain boundaries. Within the larger grains, aligned α colonies / platelets/ lamellar α, widmanstatten structure and mixed structures are observed. The complete transformation of microstructure is due to the deformation of the material above BTT and a similar observation has been reported in literatures for near α Ti alloys and α + β Ti alloys[15]. At M1, M2 and M3, depending upon the degree of deformation, the combination of transformed α in lath form and thicker grain boundary α were observed. In M3 and M4, smaller grains and thicker α at grain boundary were observed which were due to heavy deformation resulting in highly strained grains which in turn acted as nucleation sites for newer grains through recrystallisation[15]. In addition, M3 and M4 locations were at the center of the thicker section and during cooling, sufficient time was available for the transformed α platelet to grow in size by diffusion and due to slower cooling rates thicker α platelets were seen (Figure 6a) [14,26,27]. The microstructure at M6 and M7 showed completely transformed α platelets in larger grains and size of αplatelets were larger running across the grain with comparatively similar α platelet thickness. However, at other locations, smaller grains were noticed with thicker α at the grain boundary. M7 location, which is at the surface of the forging, during soaking before forging, this region had been exposed to temperature above BTT for a long time, resulted in larger grains and similar thickness α platelet (Figure 6b). While transferring the part from furnace to die, the outer surface cools faster compared to the core resulting in chilling effect as the outer surface came in contact with the die. The chilling effect caused during forging on the outer surface resulted in retaining the microsructure formed during soaking time.

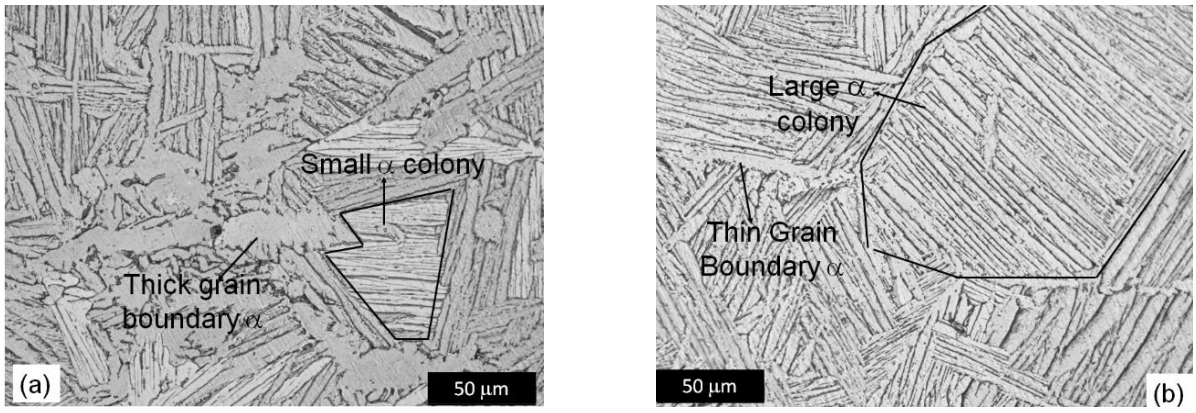

Figure 6: (a) M4 Location Microstructure of E2 Showing Transformed α along with Thicker Grain Boundary α and Smaller Grain Size Showing Slower Cooling Rate Compared to M7 (b) M7 Location Microstructure Showing Transformed α with Thinner Grain Boundary α

3.3. Heat Treated Microstructure

Figure 7 shows the heat-treated microstructure at different locations (M1 to M7) for E1 and E2 at lower magnification. Figure 8 shows the SEM image of α morphology at higher magnification in E1 and E2. Microstructure shows fully transformed α with prior β grain boundary and consists of mixed aligned α colonies in lath/ acicular form, widmanstatten, basketweave microstructure. The similar microstructure was reported in literature for similar heat treatment

cycle[14,15,21,26,28]. The α platelets form from the nucleation sites at prior β grain boundaries, triple points and other favorable nucleation sites inside the grain. α platelets form with their basal planes {0002} parallel to the {110} β planes[6]. As the α can be formed from β in 12 different variants, it leads to intersecting α colonies[29]. If there are sufficient high energy sites for nucleation within the grains, then the colonies will be narrower resulting in basketweave structure [15]. During fast cooling, nucleation and growth of transformed alpha leads to basketweave structure with shorter α platelet length compared to the α colonies which are formed with lesser cooling rate.

E1 and E2 microstructures were shown widmanstatten and basketweave structure at locations near to the surface of forging compared to the α colonies/ acicular α and needle α at the thicker section resulting from the difference in cooling rate. From the literature it is found that with increase in cooling rate, the α morphology changes from α platelet to widmanstatten and basketweave structure. With increase in cooling rate, the α platelet thickness also reduces, as also observed in the present experiments [14,15,21,26]. The variation in the morphology of the structure of α is due to the difference in the cooling rate at the surface and core of the forging. However, all the three types of α morphology are the result of an intermediate cooling rate resulting from the oil quenching[14,15]. This indicates that sufficient cooling rate has been experienced by the part so as to avoid the formation of large α lath [15].

Figure 9 shows that the average grain diameter of E1 is larger compared to the E2 at all locations. The average grain size diameter of E1 varies from 1.478 mm to 1.837mm as against 1.148mm to 1.454mm in E2. E1 microstructure shows thicker grain boundary α at many locations compared to E2 microstructure. Upon comparing the microstructures of E1 and E2 it is observed that variation in grain size is higher in E1 as compared to E2. Due to the presence of needle structure and mixed microstructure it was difficult to exactly determine the α platelet thickness. However, α platelet thickness for E1 and E2 as measured varies from 0.35μm to 3.5μm and the overall α platelet thickness of E2 is finer compared to the E1. The grain boundary thickness of both E1 and E2 as measured varies widely being less than 0.5μm in many grains and as high as 35 μm thick in a few places (Figure 10a) in E1 condition. In E2 condition, the maximum grain boundary thickness is 6μm only (Figure 10b). Overall statistics reveals that the E2 has finer grain boundaries as compared to E1 and is attributed to the difference in the number of nucleation sites available for the transformed α to form during heat treatment. As forged microstructure of E1 shows the primary α of larger α plate thickness (~ 15-20 μm) compared to the transformed α thickness of E2 (~ <10 μm). The finer α platelets during solutionising transformed to β phase considerably faster resulting in the uniform β grains. During quenching, α nucleated at different orientations as per the preferred crystallographic directions into various α colonies within the single grain. The non-uniform distribution of grains consisting of smaller grains along with larger grains are seen in E1. This could be the result of the difference in transformation rate of α phase to β phase during solutionising. As seen from the as forged microstructure of E1, primary α and low volume fraction of transformed α has led to the difference in β transformation and grain growth during solutionising.

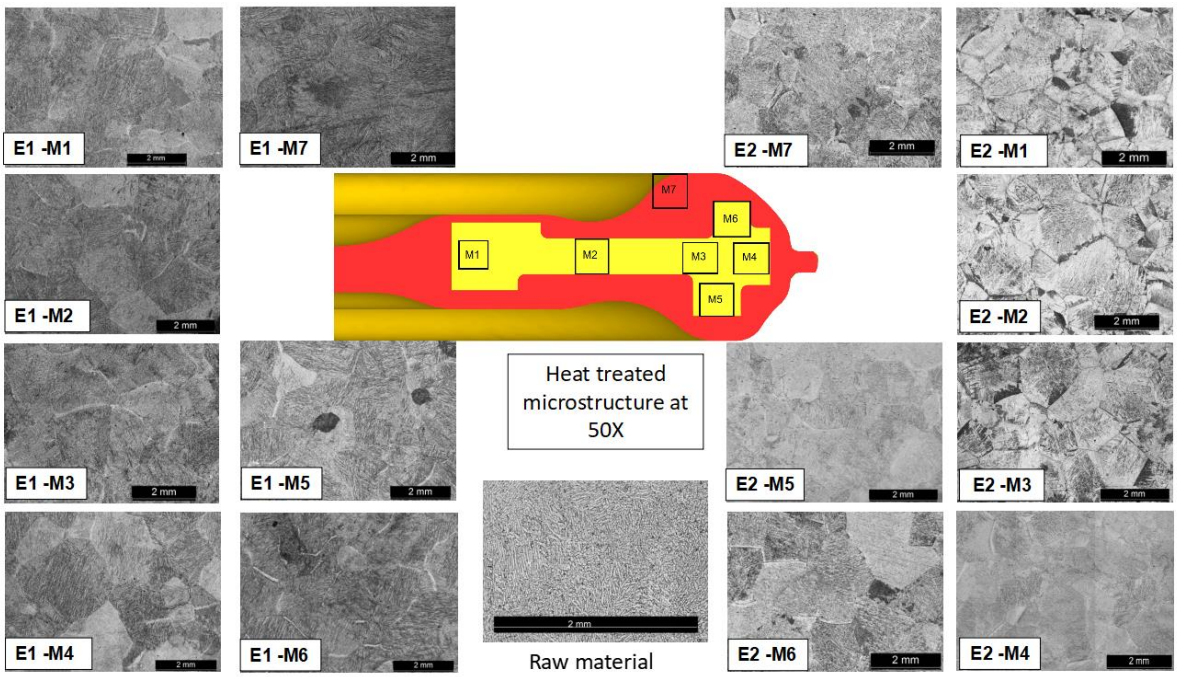

Figure 7: Heat Treated Microstructure at M1 to M7 Locations for E1 and E2 along with Raw Material Microstructure Showing Transformed *α* within Prior β Grain Boundary

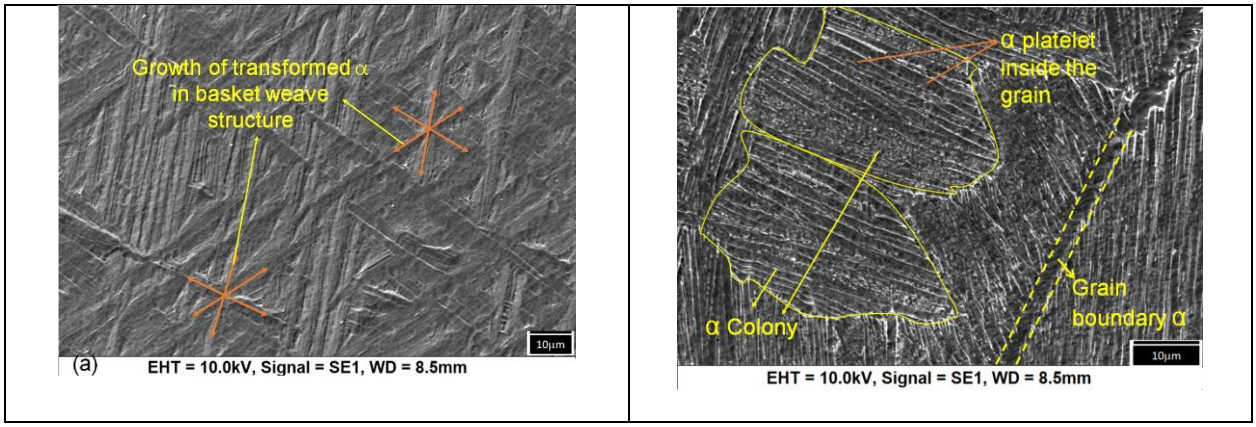

Figure 8: Typical SEM Image of (a) E1 Showing the α Platelet Morphology in Basketweave Structure and (b) E2 Showing α Platelet Morphology in Mixed Morphology (Plates and Basket Weave Structure)

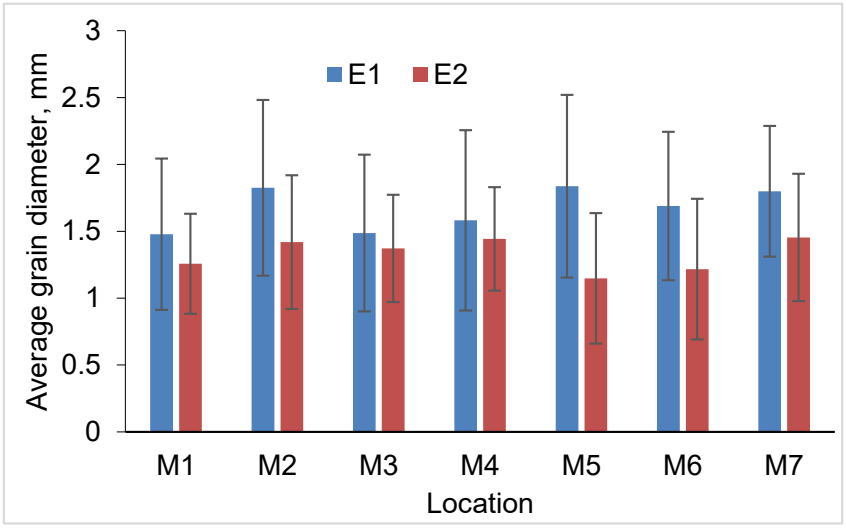

Figure 9: Average Grain Diameter of E1 and E2 at Different Locations shown with Standard Deviation of Grain Diameter as Error Bar

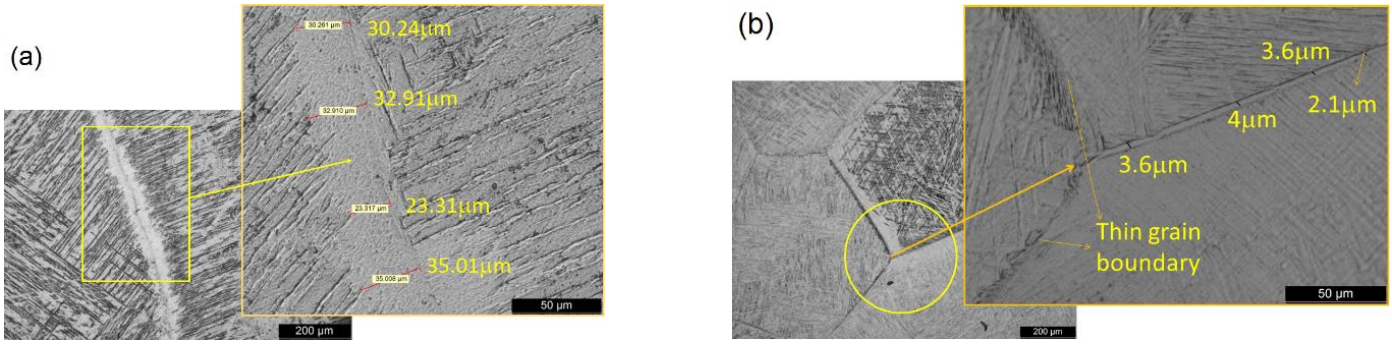

Figure 10: a) Typical Location in E1 Showing Maximum Grain Boundary α Thickness Measuring Grain Boundary α Thickness from 23μm to 35μm and b) Typical Location in E2 Showing Grain Boundary α Thickness from 2μm to 4μm

3.4. Creep Rate

Figure 11 shows the percentage of strain versus time plot generated during the creep testing and the steady state creep rate calculated using Equation 1 for E1 and E2 (3 lines correspond to 3 samples for each experiment). From Figure 11, it can be seen that after the instantaneous elongation, the creep curve falls under a steady state creep region till the completion of 100 h test duration.

$$\dot{\epsilon} = \frac{d\epsilon}{dt} \qquad \textbf{Equation 1}$$

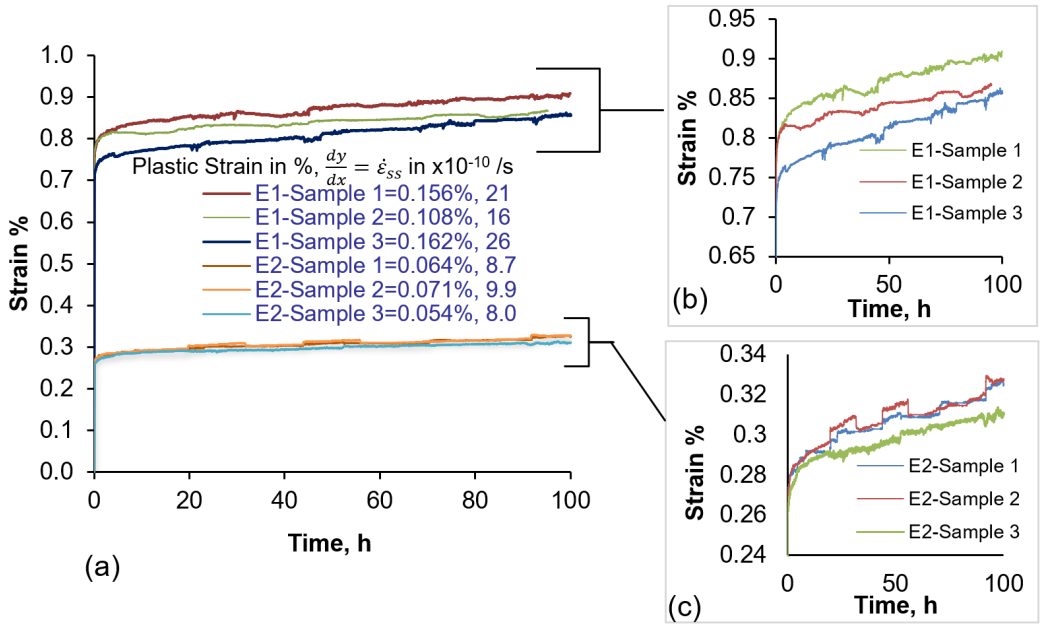

Figure 11: Creep Curve Representing Strain % Versus Time along with Steady State Creep Rate for 3 Samples each for E1 and E2

Table 3 shows the comparison of plastic strain of E1 and E2 with literature values of isothermal forging in LT26A and in IMI685[19].[Table 2 near here] From Table 2, it can be seen that the E2 plastic strain is comparable with IMI685 literature values and E2 exhibits higher creep resistance compared to E1 and LT26A isothermally forged disc. The lower creep resistance reported by Somani et al., in LT26A is due to the smaller grain size and non-uniform distribution of grain size and also the heat treatment process[19]. Essentially, the difference in creep resistance is due to the difference in the grain size and α plate distribution. E1 showed thicker grain boundaries and non-uniform grain size distribution compared to E2.

From the temperature (0.4Tm) and stress conditions (σ/G = 6 x 10^{-3}) used for testing, the creep phenomenon falls under the combination of dislocation creep / low temperature power law creep and grain boundary sliding (Deformation mechanism map (DMM) of Ti-6Al is considered as a reference as DMM for IMI 685 is not available in literature) [30]. Creep rate under steady state has been determined using the Equation 2[31] for dislocation creep.

$$\dot{\varepsilon} = B\sigma^n \exp\left(-\frac{Q}{kT}\right) \qquad \textbf{Equation 2}$$

where B and n are material constants, Q is activation energy, k is Boltzmann's constant and T is temperature in K.

Properties	Sample No.	E1	E2*	IMI685 Disc[26]	LT26A Disc[26]
Plastic strain (%) at 300 MPa for E1 and E2 and 310MPa for IMI 685 and LT26A disc	1	0.156	0.064	0.04	0.10
	2	0.108	0.071	0.05	0.14
	3	0.161	0.054	0.02	0.10
*For E1 3 samples has been tested and discontinued as the creep properties were not suitable of compressor disc application. For E2, another 17 samples were tested and their plastic strain in % are as follows: 0.04, 0.07, 0.03, 0.07, 0.04, 0.023, 0.076, 0.08, 0.09, 0.07, 0.04, 0.076,0.02, 0.031, 0.055, 0.068 and 0.08.					

Table 3: Plastic Strain Comparison of E1 and E2 with Literature Values at 520°C, 100h Duration

Grain boundary sliding has to be acting alongside any creep mechanism to maintain the grain contiguity. Creep rate for grain boundary sliding mechanism as provided by Ashby and Verral [32] is shown in Equation 3.

$$\dot{\varepsilon} = 100\frac{\Omega}{kTd^2}\left(\sigma - \frac{0.72\gamma_B}{d}\right)D_v\left(1 + \frac{3.3\delta D_B}{dD_v}\right) \quad \text{Equation 3}$$

where Ω is atomic volume, d is grain size, σ is applied stress, γ_B is grain boundary free energy, D_v is bulk diffusion coefficient, DB is boundary diffusion coefficient and δ is grain boundary thickness. Maximum grain boundary thickness for E1 is 35µm and E2 is 6 µm. The average grain diameter calculated from all the locations for E1 is 1.661mm and E2 is 1.325mm. Calculating creep rate as per Equation 3, by keeping all the common values as constant and substituting grain diameter and grain boundary thickness, it is found that E1 shows approximately 7 times higher creep strain compared to E2 if grain boundary sliding is considered as the predominant mechanism. However, the experimental values in the creep rate difference between E1 and E2 is low compared to theoretical values. This may be due to some other mechanism such as Coble creep may also be acting during creep deformation. Coble creep rate under steady state is determined using the Equation 4[33].

$$\dot{\varepsilon}_s \cong \frac{A\delta\Omega\sigma D_{gb}}{RTd^3} \quad \text{Equation 4}$$

where A is a constant (µm^{-4} /mol), δ is the width of grain boundary (µm), Ω is the atomic volume (µm^3), σ is the applied stress (N/µm^2), D_{gb} is the grain boundary self-diffusion coefficient (µm^3 /s), R = 8.314 J/mol K, T is the testing temperature (K) and d is the grain size (µm),

As per Equation 4, creep rate is the function of δ/d^3. As the creep testing condition remains the same for E1 and E2, assuming $A\Omega\sigma D_{gb}/RT$ as constant(C), then the creep rate equation reduces as given in Equation 5.

$$\dot{\varepsilon}_s = C\frac{\delta}{d^3} \quad \text{Equation 5}$$

Based on Equation 5, the observed difference in the creep rate of E1 (7.6 x 10^{-3} times Constant) is 3 times higher than the creep rate of E2 (2.57 x 10^{-3} times Constant).

Activation energy for the primary and secondary stage creep can be expressed in the form of Arrhenius type of equation at constant stress between strain rate and temperature as shown in Equation 6[31].

$$\dot{\varepsilon}_s = A\sigma^n e^{\left(-\frac{Q}{RT}\right)} \quad \text{Equation 6}$$

where A is constant, n is stress component, Q is apparent activation energy for creep, R is gas constant and T is test temperature in K. At constant stress, Q can be derived by taking log on both sides and differentiating with respect to 1/T, Equation 7 was arrived.

$$\left(\frac{\partial \ln \dot{\varepsilon}}{\partial\left(\frac{1}{T}\right)}\right)_\sigma = -\frac{Q}{R} \quad \text{Equation 7}$$

The activation energies calculated for E1 and E2 were 101kJ/mol and107kJ/mol respectively, which were in agreement with the reported value of 30 to 83kJ/mol for the Si containing Ti alloys indicating the solute drag effect is acting during creep [16]. From the strain rate equation and activation energy values it is observed that Coble creep, solute drag effect are the predominant mechanisms along with other creep mechanisms acting together.

Overall, it is established that β processing is necessary for obtaining higher creep resistance. Superior creep resistance is reported for the lamellar structure compared to equiaxed structure by many authors. This is due to the smaller α lath/ platelets which will result in smaller effective slip length. Smaller grain boundary will be beneficial for higher creep resistance as the crack propagation gets deviated at the α / α interface and at the grain boundaries. Creep resistance increases with the decrease in α platelet thickness and with an increase in discontinuous interplatelet β phase in the grain boundary[15,21]. According to Vassel et al., either β processing or β heat treatment is necessary for achieving high creep resistance and the present work "r*ecommends β processing along with β heat treatment to achieve high creep resistance for the compressor disc application where the required plastic strain percentage is less than 0.1%*".

4. Conclusions

Detailed study of the microstructure formation during forging of IMI 685 alloy, in the as forged condition and after β solutionising and aging heat treatment condition has been carried out. Based on the study the following conclusions have been arrived:

1. Plastic strain percentage of entirely α + β phase forged part was higher than the part forged in α+ β/β phase region due to the difference in grain size and the grain boundary α thickness which was the result of processing temperature.
2. Creep strain rate in the steady state creep region for α + β/β phase forged part was three times lower (better creep resistance) compared to α + β phase forged part.
3. Activation energy calculated for E1 was 101kJ/mol and E2 was 107kJ/mol. Coble creep and solute drag effect are the predominant creep mechanism acting at 520°C at a stress level of 300MPa.
4. It is recommended to forge the part in α + β phase during the initial stage followed by forging in β phase for the parts undergoing different stages during manufacturing.
5. It is recommended to forge entirely in β phase if only one stage forging is involved in the manufacturing of the forgings.

Acknowledgement

Authors thank M.S, Venkatesh, Ex-General Manager, Mr. Praveen B, General Manager (Foundry and Forge Division), Hindustan

Aeronautics Limited for providing all the necessary support and granting permission to publish this paper.

Funding

This study was funded by Foundry and Forge Division, Hindustan Aeronautics Limited, Bangalore, India.

Disclosure Statement

The authors report that there are no competing interests to declare.

Data Availability Statement

The required data has been provided in the paper.

References

1. J.R.B. Gilbert, The uses of titanium, Mater. Sci. Technol. (United Kingdom). 1 (1985) 257–262.
2. S.M. Jagadeesh Babu, B.P. Kashyap, N. Prabhu, R. Kapoor, R.N. Singh, J.K. Chakravartty, Effect of hydrogen on high temperature flow behavior of near α-Ti alloy, Mater. Sci. Eng. A. 679 (2017) 75–86.
3. X. Gao, W. Zeng, X. Li, D. Zhou, J. Xu, Q. Wang, Effect of boundary on the alpha phase precipitation in a near-alpha titanium alloy, Mater. Lett. 233 (2018) 298–301.
4. R.R. Boyer, An overview on the use of titanium in the aerospace industry, Mater. Sci. Eng. A. 213 (1996) 103–114.
5. Y. Lu, M. Aristizabal, X. Wang, B. Pang, Y.L. Chiu, Z.T. Kloenne, H.L. Fraser, M.H. Loretto, The influence of heat treatment on the microstructure and properties of HIPped Ti-6Al-4V, Acta Mater. 165 (2019) 520–527.
6. G. Lütjering, J.C. Williams, A. Gysler, Microstructure and Mechanical Properties of Titanium Alloys, Microstruct. Prop. Mater. 45 (2000) 1–77.
7. H. Li, Z. Zhao, H. Guo, Z. Yao, Y. Ning, X. Miao, M. Ge, Effect of initial alpha lamellar thickness on deformation behavior of a near-α high-temperature alloy during thermomechanical processing, Mater. Sci. Eng. A. 682 (2017) 345–353.
8. S.L. Semiatin, V. Seetharaman, I. Weiss, Flow behavior and globularization kinetics during hot working of Ti-6Al-4V with a colony alpha microstructure, Mater. Sci. Eng. A. 263 (1999) 257–271.
9. H. Li, Z. Zhao, Y. Ning, H. Guo, Z. Yao, Characterization of microstructural evolution for a near-α Titanium alloy with different initial lamellar microstructures, Metals (Basel). 8 (2018).
10. E.B. Shell, S.L. Semiatin, Effect of initial microstructure on plastic flow and dynamic globularization during hot working of Ti-6AI-4V, Metall. Mater. Trans. A Phys. Metall. Mater. Sci. 30 (1999) 3219–3229.
11. S.L. Semiatin, T.R. Bieler, The effect of alpha platelet thickness on plastic flow during hot working of Ti-6Al-4V with a transformed microstructure, Acta Mater. 49 (2001) 3565–3573.
12. S.L. Semiatin, T.R. Bieler, Effect of texture and slip mode on the anisotropy of plastic flow and flow softening during hot working of Ti-6Al-4V, Metall. Mater. Trans. A. 32 (2001) 1787–1799.
13. R. Filip, K. Kubiak, W. Ziaja, J. Sieniawski, The effect of microstructure on the mechanical properties of two-phase titanium alloys, J. Mater. Process. Technol. 133 (2003) 84–89.
14. D.F. Blenkinsop, P. A., Neal, R.E. Goosey, Effect of Heat Treatment on the Microstructure and Properties of IMI 685, Titan. Titan. Alloy. Proc. 3rd Int. Conf. Titan. (1982) 2003–2014.
15. Z.X. Guo, T.N. Baker, On the microstructure and thermomechanical processing of titanium alloy IMI685, Mater. Sci. Eng. A. 156 (1992) 63–76.
16. T.K. Assadi, H.M. Flower, D.R.F. West, Creep resistance of certain alloys of the Ti–AI–Zr–Mo–Si system, Met. Technol. 6 (1979) 16–23.
17. Y. Liu, T.N. Baker, Deformation characteristics of IMI685 titanium alloy under β isothermal forging solutions, Mater. Sci. Eng. A. 197 (1995) 125–131.
18. V.G. Krishna, Y.V.R.K. Prasad, N.C. Birla, G.S. Rao, Processing map for the hot working of near-α titanium alloy 685, J. Mater. Process. Technol. 71 (1997) 377–383.
19. M.C. Somani, R. Sundaresan, O.A. Kaibyshev, A.G. Ermatchenko, Deformation processing in superplasticity regime-production of aircraft engine compressor discs out of titanium alloys, Mater. Sci. Eng. A. 243 (1998) 134–139.
20. Barbier, F., Quesne, C., Servant, C., & Lacombe, P. (1981). Relations Between the Microstructure and Tensile and Creep Properties of Titanium Alloy Ti 685; Influence of Cooling Rate and Different Forging Conditions. *J. Less Common Met., 79*(1), 75-95.
21. A.G. A.Vassel, F.H. Froes, J.P. Herteman, D.Eylon, Influence of Processing and Heat Treatment Variables on the Mechanical Properties of Two Advanced High Temperature Titanium Alloys, in: G. Lutjering, U. Zwicker, W. Bunk (Eds.), Titanium, Sci. Technol., DEUTSCHE GESELLSCHAFT FOR METALLKUNDE E.V, 1985: pp. 515–521.
22. A. Jayanthi, M. Anilkumar, B. Ravisankar, Selection of forging process for compressor disc for aero engine using finite element analysis, Mater. Today Proc. 60 (2022) 2111–2116.
23. A. Jayanthi, M. Anilkumar, B. Ravisankar, Study on multi stage forging process with combination of different strain rate and temperature region in IMI685 aero engine compressor disc forging, Mater. Today Proc. 60 (2022) 1973–1980.
24. P. Gao, M. Zhan, X. Fan, Z. Lei, Y. Cai, Hot deformation behavior and microstructure evolution of TA15 titanium alloy with nonuniform microstructure, Mater. Sci. Eng. A. 689 (2017) 243–251.
25. S.L. Semiatin, An Overview of the Thermomechanical Processing of α/β Titanium Alloys: Current Status and Future Research Opportunities, Metall. Mater. Trans. A Phys. Metall. Mater. Sci. 51 (2020) 2593–2625.
26. V. Singh, C. Ramachandra, Effect of Heat Treatment on Microstructure and Mechanical Properties of Titanium Alloy IMI685., Key Eng. Mater. A8 (1985) 185–202.
27. N. Kherrouba, M. Bouabdallah, R. Badji, D. Carron, M. Amir, Beta to alpha transformation kinetics and microstructure of Ti-6Al-4V alloy during continuous cooling, Mater. Chem.

Phys. 181 (2016) 462–469.
28. S. Denis, J.C. Chevrier, G. Beck, Étude des contraintes résiduelles introduites par la trempe dans des cylindres en TA6ZrD (685), J. Less-Common Met. 69 (1980) 265–276.
29. D. Banerjee, J.C. Williams, Perspectives on titanium science and technology, Acta Mater. 61 (2013) 844–879.
30. K. Janghorban, S. Esmaeili, Deformation-mechanism map for Ti-6wt% Al alloy, J. Mater. Sci. 26 (1991) 3362–3365.
31. Weertman, J. (1960). Creep of indium, lead, and some of their alloys with various metals. *Trans. Met. Soc. AIME*, 218.
32. M.F. Ashby, R.A. Verrall, Diffusion-accommodated flow and superplasticity, Acta Metall. 21 (1973) 149–163.
33. R.L. Coble, A Model for Boundary Diffusion Controlled Creep in Polycrystalline Materials, J. Appl. Phys. 34 (1963) 1679–1682.